Nanoscale Advances

ROYAL SOCIETY OF CHEMISTRY

PAPER

View Article Online
View Journal | View Issue

Check for updates

Cite this: *Nanoscale Adv.*, 2020, **2**, 5682

Gas–solid two-phase flow (GSF) mechanochemical synthesis of dual-metal–organic frameworks and research on electrochemical properties†

Jun Zhao, [ab] Bo Jin [*a] and Rufang Peng[*a]

Received 6th September 2020
Accepted 19th October 2020

DOI: 10.1039/d0na00749h

rsc.li/nanoscale-advances

As an alternative approach for conventional mechanochemical synthesis, a novel gas–solid two-phase flow (GSF) synthetic technique for the mechanochemical synthesis of dual metal–organic frameworks (DMOFs) was reported for the first time. The prepared $CoMn_2(BTC)_2$ was characterized by FT-IR, DTA, TG/DTG, and XRD studies. The results indicated that $CoMn_2(BTC)_2$ (BTC = 1,3,5-benzenetricarboxylate) was successfully synthesized after 10 min at a rate of 60 kg h^{-1}. $CoMn_2O_4$ microspheres were also prepared *via* the $CoMn_2(BTC)_2$ precursor method and characterized using FT-IR, XPS, XRD, SEM, EDS, and BET methods. The electrochemical properties of the as-prepared $CoMn_2O_4$ were investigated, and the GSF results showed that the microsphere electrodes of $CoMn_2O_4$ had a high specific capacitance (969 F g^{-1}) at a current density of 1 A g^{-1} in 3 M aqueous KOH solution.

Open Access Article. Published on 20 October 2020. Downloaded on 12/4/2025 1:56:37 PM.
This article is licensed under a Creative Commons Attribution-NonCommercial 3.0 Unported Licence.

Introduction

Bimetallic oxides have been extensively studied and are considered a candidate for lithium-ion battery (LIB) anode materials because of their higher theoretical specific capacity than graphite, low cost, and environmental benignity. In particular, $CoMn_2O_4$ has the advantages of cobalt- and manganese-based metal oxides and superior application in the field of LIBs.[1,2]

The precursor method was one of the main methods to prepare $CoMn_2O_4$. Usually, sodium hydroxide or acid citrate is used to provide coordination sites, and cobalt and manganese are added to form a complex at high temperature and high pressure by the solvothermal method. Then, the obtained complex is burned to prepare the target product. However, this traditional method requires the extensive use of hostile organic solvents, thereby increasing environmental burden. Moreover, it is impossible to achieve the process conditions of batch preparation.

In this study, we used dual metal–organic frameworks (DMOFs) [$CoMn_2(BTC)_2$] as the precursor of $CoMn_2O_4$.[3–12] Before mechanochemical synthesis,[13–17] DMOFs were also prepared through the conventional solvohermal method. Nowadays, MOFs are realized by mechanical ball milling and twin-screw extrusion. However, these synthetic techniques suffer from many drawbacks, such as time and energy consumption.[18–20] Thus, the development of a novel mechanochemical synthetic technique is highly desirable.

This work explored the use of a gas–solid two-phase flow (GSF) (Fig. 1) for the mechanochemical synthesis of DMOFs (Fig. S5† shows the reaction process flow chart of the GSF). The results indicated that $CoMn_2(BTC)_2$ (BTC = 1,3,5-benzenetricarboxylate) was successfully synthesized. $CoMn_2(BTC)_2$ was also used as a precursor to prepare $CoMn_2O_4$ microspheres, and their electrochemical properties were studied.

Experimental

Chemicals and materials

Cobaltous nitrate ($Co(NO_3)_2 \cdot 6H_2O$, AR, 98.0%) and manganous acetate ($Mn(CH_3COO)_2$, AR, 99%) were purchased from Kelong

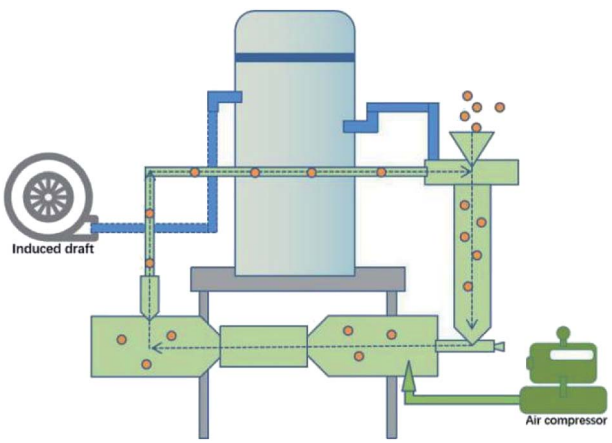

Fig. 1 The reaction process flow chart of the GSF.

[a]*State Key Laboratory Cultivation Base for Nonmetal Composites and Functional Materials, Southwest University of Science and Technology, Mianyang 621010, China*
[b]*Sichuan College of Architecture and Technology, Deyang, 618000, China*

† Electronic supplementary information (ESI) available: The prepared $CoMn_2(BTC)_2$ was characterized by FT-IR, DTA, TG/DTG, and XRD studies (Fig. S1–S4). See DOI: 10.1039/d0na00749h

This journal is © The Royal Society of Chemistry 2020

Open Access Article. Published on 20 October 2020. Downloaded on 12/4/2025 1:56:37 PM.
This article is licensed under a Creative Commons Attribution-NonCommercial 3.0 Unported Licence.

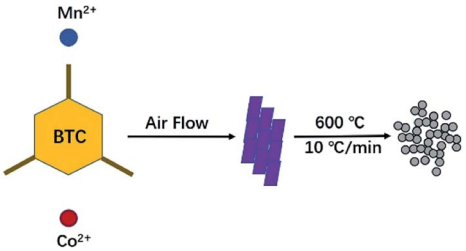

Scheme 1 Preparation of $CoMn_2O_4$ with a controlled composition and size.

(Chengdu, China). 1,3,5-Trimesic acid (H_3BTC), was purchased from Aladdin (Shanghai, China). Fourier transform infrared (FT-IR) spectra were recorded on a Nicolet-5700 FTIR spectrometer using pressed KBr pellets to test the chemical bonding of the samples from 4000 to 400 cm^{-1}. X-ray photoelectron spectroscopy (XPS) experiments were carried out using an XPS-7000 spectrometer with Al Kα radiation. Thermogravimetric analysis (TGA) was carried out on a TGA 4000 (Perkin Elmer Co., Ltd) with the temperature range from room temperature to 600 °C in air. Differential thermal analysis (DTA) curves were recorded on a WCR-1B instrument in flowing air at a heating rate of 10 °C min^{-1}. Field-emission scanning electron microscopy (FESEM) measurements were performed on an Ultra 55 microscope (ZEISS Company, The German) with an acceleration voltage of 15.0 kV with energy dispersive spectroscopy (EDS) detectors. XRD was performed on a Philips X'Pert Pro X-ray diffractometer (PANalytical, Holland). The N_2 adsorption–desorption tests were performed on a Micromeritics ASAP 2460 instrument.

Synthesis of $CoMn_2(BTC)_2$

$CoMn_2(BTC)_2$ was prepared as follows. $Co(NO_3)_2 \cdot 6H_2O$ (1.309 kg), $Mn(CH_3COO)_2$ (0.805 kg) and H_3BTC (1.38 kg) were mixed, and the mixture was transferred into an impact chamber at the rate of 1 kg min^{-1} (60 kg h^{-1}). Then, the materials were accelerated to supersonic velocity with compressed air (1.5 MPa).[21] The products were collected after different reaction times. Here, 1.68 kg of the purple crystal were collected after 10 min. Yields: 91% based on H_3BTC.

Precursor method for the synthesis of $CoMn_2O_4$ microspheres

$CoMn_2O_4$ was prepared as shown in Scheme 1. The as-prepared $CoMn_2(BTC)_2$ was placed in a tube furnace and heated to 600 °C at a temperature increase rate of 10 °C min^{-1} in air, and maintained at this temperature for 12 h, then cooled down to room temperature, and the $CoMn_2O_4$ microspheres were obtained.[22–25]

Results and discussion

Characterization

Fig. 2 shows the FT-IR spectrum of $CoMn_2O_4$. Similar to the results reported in the literature, the peaks at 3412 and 1628 cm^{-1} originated from a hydroxyl group in the form of

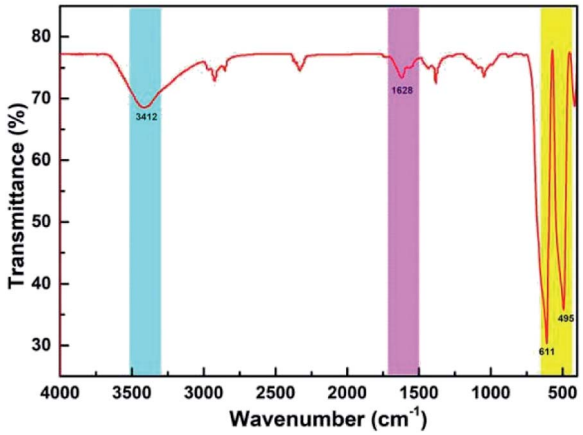

Fig. 2 Fourier transform infrared (FT-IR) spectra of $CoMn_2O_4$.

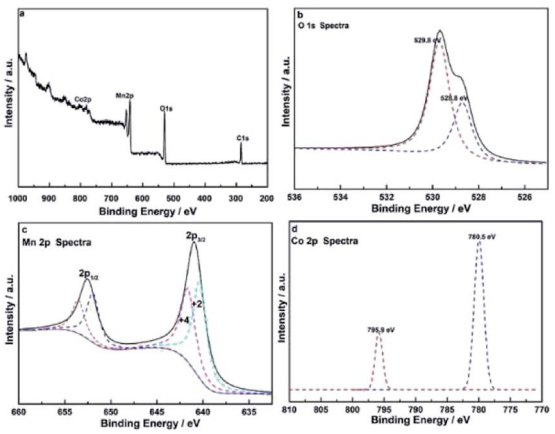

Fig. 3 (a) High-resolution XPS spectra of (b) deconvoluted O 1s, (c) Co 2p, and (d) Mn 2p of $CoMn_2O_4$.

physically adsorbed water.[26–28] The two peaks at 611 and 495 cm^{-1} corresponded to the Mn–O and the Co–O bonds.

Fig. 3a illustrates the XPS survey.[29] Fig. 3b shows that the O 1s peak was at 529.8 and 528.8 eV. A hybrid of the two peaks with Gaussian fitting was used to obtain the amount of points for calculation of the two peaks. The peaks at 529.8 and 528.8 eV represented the Mn–O–Mn and the Mn–OH bonds, respectively. Cobalt oxide was negligible because the quantity of the doped cobalt was low. The Mn–O–Mn and the Mn–OH bonds were related to MnO_2 and Mn_2O_3, respectively. As such, the manganese oxide (Fig. 3c) in $CoMn_2O_4$ was mixed with MnO_2 and Mn_2O_3 at 29.81% and 70.19%, respectively, on the basis of the peak separation results. The valence of manganese oxide was less than quadrivalent, and its oxidation state was 2.6. Fig. 3d shows the Co $2p_{1/2}$ and Co $2p_{3/2}$ peaks at 780.5 and 795.9 eV, which was consistent with the Co 2p orbital peak of Co_3O_4. Thus, Co, existing in the form of a Co_3O_4 spinel structure, can cause lattice distortion in the manganese oxide mixture and increase surface spacing, making it easier to conduct ions into the manganese oxide.[30]

Fig. S6 and S7† show the XRD patterns of the product collected at different times and after TGA, respectively. As

Open Access Article. Published on 20 October 2020. Downloaded on 12/4/2025 1:56:37 PM.
This article is licensed under a Creative Commons Attribution-NonCommercial 3.0 Unported Licence.

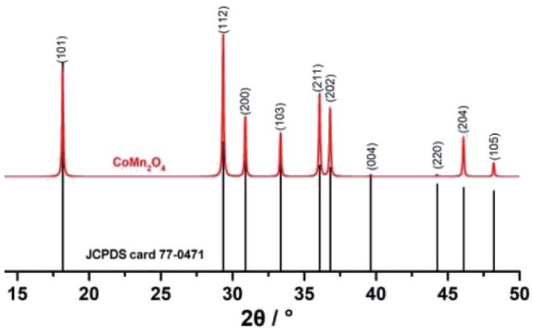

Fig. 4 XRD pattern of $CoMn_2O_4$ and the standard diffraction pattern of $CoMn_2O_4$ (JCPDS card no. 77-0471).

illustrated in Fig. 4, the XRD pattern can be readily assigned to the body-centered tetragonal $CoMn_2O_4$ (JCPDS card no. 77-0471), which showed good properties.[31] The absence of the characterization peaks from residues or other contaminants indicated the high purity of the products.

The electrochemical performance of active materials is greatly related to the morphology and assembled structures. Consequently, the formation of nanosheet assembled microspheres is distinctly important to the electrochemical performance of $CoMn_2O_4$. The hybrids were investigated by field-emission scanning electron microscopy to obtain the microscopic structure of $CoMn_2O_4$, explore its application value, and further illustrate $CoMn_2O_4$ synthesis. Fig. 5a shows the typical SEM image of the obtained $CoMn_2O_4$ in the form of a regular microsphere. As shown in Fig. 5b, the microsphere showed plate-like particles when we further enlarged the surface of $CoMn_2O_4$. The surface of the $CoMn_2O_4$ microsphere was smooth and had many micropores. Meanwhile, the chemical analysis conducted *via* EDS revealed the compositional signals for Co, Mn, and O, as confirmed by the elemental mapping images (Fig. 5c–f).[32]

Nitrogen adsorption/desorption isotherms were obtained at 77 K to study the textural properties of $CoMn_2O_4$. Because of its

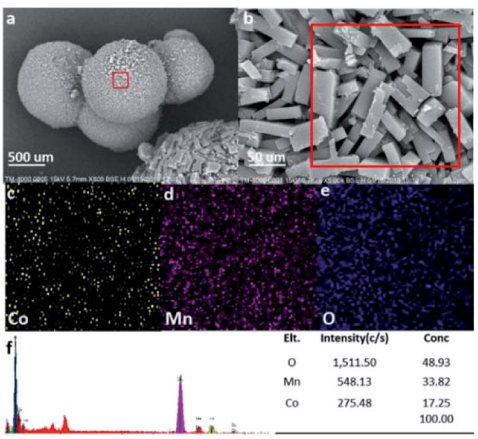

Fig. 5 (a and b) SEM images of $CoMn_2O_4$, (c–e) elemental mapping images, and (f) corresponding elemental contents measured by energy dispersive spectroscopy.

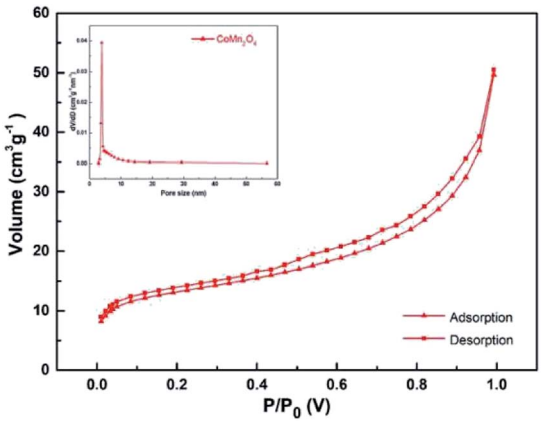

Fig. 6 N_2 adsorption/desorption isotherms of $CoMn_2O_4$.

spherical structure, its specific surface area was large. Based on the nitrogen adsorption–desorption curves, the BET surface area of $CoMn_2O_4$ (ref. 33) (Fig. 6) was 63.3 $m^2\ g^{-1}$ (Fig. S8† shows the BET surface area of $CoMn_2(BTC)_2$).

Supercapacitive properties

The electrochemical properties of the as-carbonized materials were evaluated in the context of supercapacitors. For a three-electrode system in 3 M aqueous KOH solution, a Ag/AgCl electrode (0.22233 V) and Pt plates were used as reference and counter electrodes, respectively. A free-standing $CoMn_2O_4$ film with a thickness of about 0.2 mm served directly as the working electrode and was prepared by pressing the $CoMn_2O_4$ film (2.65 mg) onto a piece of copper foam (1 cm × 1 cm). Cyclic voltammetry (CV) and chronopotentiometry measurements were conducted at various scan rates (0.0–0.8 V) and current densities (1–20 A g^{-1}), respectively. Benefiting from the porous microsphere structures, the $CoMn_2O_4$ electrodes were subjected to CV tests to evaluate their electrochemical behavior in 3 M aqueous KOH solution, as shown in Fig. 7.

The CV curves were measured at scan rates between 5 and 100 mV s^{-1} within a potential window of 0.0–0.8 V (*vs.* Ag/AgCl),

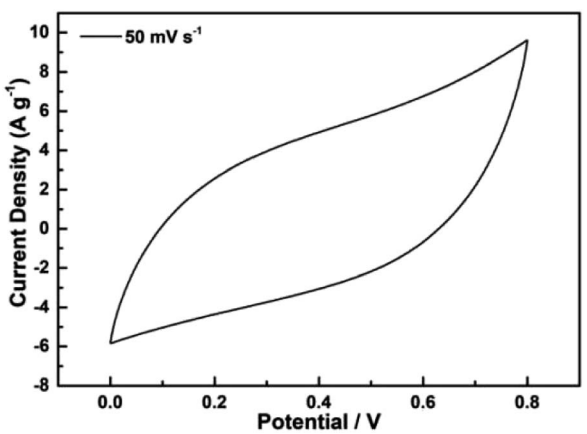

Fig. 7 Cyclic voltammetry curve of $CoMn_2O_4$ electrodes obtained using the three-electrode method at a voltage scan rate of 50 mV s^{-1}.

This journal is © The Royal Society of Chemistry 2020

Open Access Article. Published on 20 October 2020. Downloaded on 12/4/2025 1:56:37 PM.
This article is licensed under a Creative Commons Attribution-NonCommercial 3.0 Unported Licence.

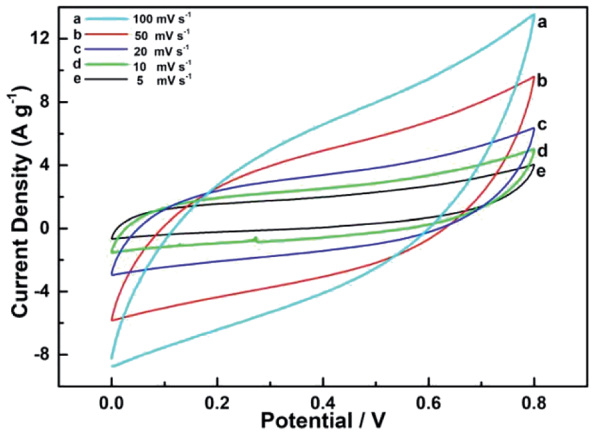

Fig. 8 Cyclic voltammetry curve of supercapacitors with $CoMn_2O_4$ as the electrode at scan rates of (a) 100, (b) 50, (c) 20, (d) 10, and (e) 5 mV s^{-1}.

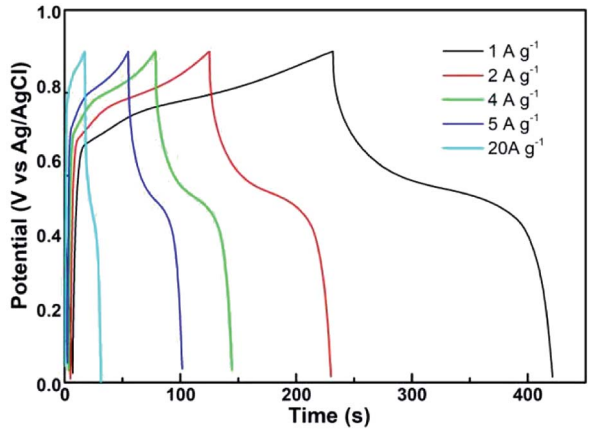

Fig. 9 Constant current charge/discharge curves of supercapacitors with $CoMn_2O_4$ as the electrode at different current densities.

as shown in Fig. 8. Typical cathodic and anodic peaks were observed during the redox reaction between $CoMn_2O_4$ and MnO–CoO. The well-developed CV curve of $CoMn_2O_4$ exhibited the largest integral area, demonstrating that $CoMn_2O_4$ possessed the best supercapacitive behavior among the three electrodes. Meanwhile, two pairs of redox peaks were associated with the Faraday effect at 0.38 and 0.45 V and 0.08 and 0.58 V of the CV curve. The quasiregular rectangle shapes also confirmed the excellent supercapacitive nature of $CoMn_2O_4$.

The supercapacitive properties[34] of $CoMn_2O_4$ were used for the subsequent method. Specific capacitance was calculated from various current densities by using the following equation:

$$C = \frac{I \times \Delta t}{m \times \Delta V} \quad (1)$$

where I (A) represents the discharge current, Δt (s) refers to the discharge time within the potential change ΔV (V), and m is the active material weight in the working electrode. All electrochemical measurements were carried out using a CHI660C (Shanghai, China) electrochemical working station.

Table 1 Specific capacitance of $CoMn_2O_4$ for different methods

Sample	Current density	Specific capacitance	Ref.
$CoMn_2O_4$ microspheres	1 A g^{-1}	969 F g^{-1}	This work
$CoMn_2O_4$ spinel material	1 A g^{-1}	188 F g^{-1}	Ren L. *et al.*[35]
$CoMn_2O_4$ electrode	5 V s^{-1}	700 F g^{-1}	Vigneshwaran P. *et al.*[36]

Fig. 9 shows the results of the constant current charge and discharge test of the $CoMn_2O_4$ supercapacitor in a voltage window of 1 V. The charge and discharge currents were 20, 5, 4, 2, and 1 A g^{-1}. The supercapacitors with $CoMn_2O_4$ electrodes can be used as charge storage devices. When the current decreased, the specific capacity of $CoMn_2O_4$ ultracapacitors increased because the electrode process was limited by the diffusion and transfer rates of the charge and ion. The electrode material cannot be fully utilized, and its capacity was reduced when the diffusion and transfer rates of the charge and ion were not as fast as the rate of the charge flow. For comparison with different methods reported before, the results are listed in Table 1. A maximum specific capacitance of 969 F g^{-1} was obtained after charging and discharging at a current density of 1 A g^{-1}.

Conclusion

The GSF method provided a new route for the mechanochemical synthesis of DMOFs, and is the successor and developed model of traditional solid phase synthesis methods. The GSF method overcame the defects in traditional solid-phase synthesis and achieved more efficient preparation. Thus, the GSF can be a novel and effective technique for the mechanochemical synthesis of DMOFs under solvent-free conditions. $CoMn_2(BTC)_2$ was successfully synthesized to confirm the feasibility of this method.[35–40] $CoMn_2O_4$ microspheres were successfully prepared *via* the $CoMn_2(BTC)_2$ precursor method, and further exploration was carried out in the application. The results showed that $CoMn_2O_4$ had good capacitive behavior when used as a supercapacitor electrode. A specific capacitance of 969 F g^{-1} was obtained after charging and discharging at a current density of 1 A g^{-1}.[41–45]

Conflicts of interest

The authors declare no conflicts of interest.

Acknowledgements

We are grateful for financial support from the National Natural Science Foundation of China (project no. 51972278), Major Frontier Innovation Project of Science and Technology Department of Sichuan Province (project no. 2019YJ0447), and Project of State Key Laboratory of Environment-friendly Energy Materials, Southwest University of Science and Technology (19 fksy04).

Open Access Article. Published on 20 October 2020. Downloaded on 12/4/2025 1:56:37 PM.
This article is licensed under a Creative Commons Attribution-NonCommercial 3.0 Unported Licence.

References

1 M. X. Li, Y. X. Yin, C. J. Li, F. Z. Zhang, L. J. Wan, S. L. Xu and D. G. Evansa, Well-dispersed bi-component-active CoO/$CoFe_2O_4$ nanocomposites with tunable performances as anode materials for lithium-ion batteries, *Chem. Commun.*, 2012, **48**(3), 410–412.

2 X. J. Hou, X. F. Wang, B. Liu, Q. F. Wang, T. Luo, D. Chen and G. Z. Shen, Hierarchical $MnCo_2O_4$ nanosheet arrays/carbon cloths as integrated anodes for lithium-ion batteries with improved performance, *Nanoscale*, 2014, **6**(15), 8858–8864.

3 J. Y. Zheng, X. L. Cui, Q. W. Yang, Q. L. Ren, Y. W. Yang and H. B. Xing, Shaping of ultrahigh-loading MOF pellet with a strongly anti-tearing binder for gas separation and storage, *Chem. Eng. J.*, 2018, **354**, 1075–1082.

4 J. R. Li, R. J. Kuppler and H. C. Zhou, Selective gas adsorption and separation in metal–organic frameworks, *Chem. Soc. Rev.*, 2009, **38**(5), 1477–1504.

5 T. Rodenas, I. Luz, G. Prieto, B. Seoane, H. Miro, A. Corma, F. Kapteijn, X. Francesc, L. Xamena and J. Gascon, Metal–organic framework nanosheets in polymer composite materials for gas separation, *Nat. Mater.*, 2015, **14**(1), 48.

6 H. L. Wang, Q. L. Zhu, R. Q. Zou and Q. Xu, Metal-organic frameworks for energy applications, *Chem*, 2017, **2**(1), 52–80.

7 H. L. Li, M. Eddaoudi, M. O'Keeffe and O. M. Yaghi, Design and synthesis of an exceptionally stable and highly porous metal-organic framework, *Nature*, 1999, **402**(6759), 276.

8 G. Y. Xu, P. Nie, H. Dou, B. Ding, L. Y. Li and X. G. Zhang, Exploring metal organic frameworks for energy storage in batteries and supercapacitors, *Mater. Today*, 2017, **20**(4), 191–209.

9 L. Wang, Y. Z. Han, X. Feng, J. W. Zhou, P. F. Qi and B. Wang, Metal–organic frameworks for energy storage: Batteries and supercapacitors, *Coord. Chem. Rev.*, 2016, **307**, 361–381.

10 D. Yang and B. C. Gates, Catalysis by metal organic frameworks: perspective and suggestions for future research, *ACS Catal.*, 2019, **9**(3), 1779–1798.

11 J. Y. Lee, O. K. Farha, J. Roberts, K. A. Scheidt, S. T. Nguyena and J. T. Hupp, Metal–organic framework materials as catalysts, *Chem. Soc. Rev.*, 2009, **38**(5), 1450–1459.

12 Y. Hua, X. X. Li, C. Y. Chen and H. Pang, Cobalt based metal-organic frameworks and their derivatives for electrochemical energy conversion and storage, *Chem. Eng. J.*, 2019, **370**, 37–59.

13 L. Takacs, The historical development of mechanochemistry, *Chem. Soc. Rev.*, 2013, **42**(18), 7649–7659.

14 P. Baláž, M. Achimovičová, M. Baláž, P. Billik, Z. C. Zheleva, J. M. Criado, F. Delogu, E. Dutková, E. Gaffet, F. J. Gotor, R. Kumar, I. Mitov, T. Rojac, M. Senna, A. Streletskiikl and K. W. Ciurowam, Hallmarks of mechanochemistry: from nanoparticles to technology, *Chem. Soc. Rev.*, 2013, **42**(18), 7571–7637.

15 S. L. James, C. J. Adams, C. Bolm, D. Braga, P. Collier, T. Friščić, F. Grepioni, K. D. M. Harris, G. Hyett, W. Jones, A. Krebs, J. Mack, L. Maini, A. G. Orpen, I. P. Parkin, W. C. Shearouse, J. W. Steed and D. C. Waddell, Mechanochemistry: opportunities for new and cleaner synthesis, *Chem. Soc. Rev.*, 2012, **41**(1), 413–447.

16 D. E. Crawford, J. Casaban, R. Haydon, N. Giri, T. McNally and S. L. James, Synthesis by extrusion: continuous, large-scale preparation of MOFs using little or no solvent, *Chem. Sci.*, 2015, **6**(3), 1645–1649.

17 G. W. Wang, Mechanochemical organic synthesis, *Chem. Soc. Rev.*, 2013, **42**(18), 7668–7700.

18 T. Panda, S. Horike, K. Hagi, N. Ogiwara, K. Kadota, T. Itakura, M. Tsujimoto and S. Kitagawa, Mechanical Alloying of Metal-Organic Frameworks, *Angew. Chem.*, 2017, **129**(9), 2453–2457.

19 T. D. Bennett, P. J. Saines, D. A. Keen, J. C. Tan and A. K. Cheetham, Ball-Milling-Induced Amorphization of Zeolitic Imidazolate Frameworks (ZIFs) for the Irreversible Trapping of Iodine, *Chem. - Eur. J.*, 2013, **19**(22), 7049–7055.

20 D. E. Crawford and J. Casaban, Recent developments in mechanochemical materials synthesis by extrusion, *Adv. Mater.*, 2016, **28**(27), 5747–5754.

21 B. Sun, Y. He, R. Peng, S. J. Chu and J. Zuo, Air-flow impacting for continuous, highly efficient, large-scale mechanochemical synthesis: a proof-of-concept study, *ACS Sustainable Chem. Eng.*, 2016, **4**(4), 2122–2128.

22 L. Zhou, D. Zhao and X. W. Lou, Double-shelled $CoMn_2O_4$ hollow microcubes as high-capacity anodes for lithium-ion batteries, *Adv. Mater.*, 2012, **24**(6), 745–748.

23 L. Wang, X. Zhao, Y. H. Lu, M. W. Xu, D. W. Zhang, R. S. Ruoff, K. J. Stevenson and J. B. Goodenough, $CoMn_2O_4$ spinel nanoparticles grown on graphene as bifunctional catalyst for lithium-air batteries, *J. Electrochem. Soc.*, 2011, **158**(12), A1379–A1382.

24 M. Prabu, P. Ramakrishnan and S. Shanmugam, $CoMn_2O_4$ nanoparticles anchored on nitrogen-doped graphene nanosheets as bifunctional electrocatalyst for rechargeable zinc-air battery, *Electrochem. Commun.*, 2014, **41**, 59–63.

25 J. Du, C. C. Chen, F. Y. Cheng and J. Chen, Rapid synthesis and efficient electrocatalytic oxygen reduction/evolution reaction of $CoMn_2O_4$ nanodots supported on graphene, *Inorg. Chem.*, 2015, **54**(11), 5467–5474.

26 C. X. Li, C. B. Chen, J. Y. Lu, S. Cui, J. Li, H. Q. Liu, W. W. Li and F. Zhang, Metal organic framework-derived $CoMn_2O_4$ catalyst for heterogeneous activation of peroxymonosulfate and sulfanilamide degradation, *Chem. Eng. J.*, 2018, **337**, 101–109.

27 L. Zhang, G. He, S. Lei, G. S. Qi, H. F. Jiu and J. Wang, Hierarchical hollow microflowers constructed from mesoporous single crystalline $CoMn_2O_4$ nanosheets for high performance anode of lithium ion battery, *J. Power Sources*, 2016, **326**, 505–513.

28 J. L. Digol, M. F. M. Labata, M. F. Divinagracia and J. D. Ocon, $CoMn_2O_4$ Anchored on N-Doped High-Dimensional Hierarchical Porous Carbon Derived from Biomass for Bifunctional Oxygen Electrocatalysis, *ECS Trans.*, 2017, **77**(11), 525–531.

29 S. Alkhalaf, C. K. Ranaweera, P. K. Kahol, H. Adhikari, S. R. Mishra, F. Perez, B. K. Gupta, K. Ramasamy and

 This journal is © The Royal Society of Chemistry 2020

Open Access Article. Published on 20 October 2020. Downloaded on 12/4/2025 1:56:37 PM.
This article is licensed under a Creative Commons Attribution-NonCommercial 3.0 Unported Licence.

R. K. Gupta, Electrochemical energy storage performance of electrospun $CoMn_2O_4$ nanofibers, *J. Alloys Compd.*, 2017, **692**, 59–66.

30 H. Zhu, D. Yu, S. G. Zhang, J. W. Chen, W. B. Wu, M. Wan, L. Wang, M. Zhang and M. L. Du, Morphology and structure engineering in nanofiber reactor: tubular hierarchical integrated networks composed of dual phase octahedral $CoMn_2O_4$/carbon nanofibers for water oxidation, *Small*, 2017, **13**(26), 1700468.

31 P. Mahata, D. Sarma, C. Madhu, A. Sundaresen and S. Natarajan, $CoMn_2O_4$ spinel from a MOF: synthesis, structure and magnetic studies, *Dalton Trans.*, 2011, **40**(9), 1952–1960.

32 Y. Y. Fu, X. Z. Lu, K. Wan, Y. X. Zhang, Y. H. Yang, H. L. Quan, X. T. Xu and F. Wang, Spinel $CoMn_2O_4$ nanosheet arrays grown on nickel foam for high-performance supercapacitor electrode, *Appl. Surf. Sci.*, 2015, **357**, 2013–2021.

33 J. Cheng, X. Liu, Y. Lu, X. Y. Hou, H. Lei, H. L. Yan, J. Y. Xu and Y. S. Luo, Porous $CoMn_2O_4$ microspheres as advanced pseudocapacitive materials, *Mater. Lett.*, 2016, **165**, 231–234.

34 Q. Li, J. N. Guo, D. Xu, J. Q. Guo, X. Ou, Y. Hu, H. J. Qi and F. Yan, Electrospun N-Doped Porous Carbon Nanofibers Incorporated with NiO Nanoparticles as Free-Standing Film Electrodes for High-Performance Supercapacitors and CO_2 Capture, *Small*, 2018, **14**(15), 1704203.

35 L. Ren, J. Chen, X. Q. Wang, M. J. Zhi, J. W. Wu and X. H. Zhang, Facile synthesis of flower-like $CoMn_2O_4$ microspheres for electrochemical supercapacitors, *RSC Adv.*, 2015, **5**(39), 30963–30969.

36 P. Vigneshwaran, M. Kandiban, N. S. Kumar, V. Venkatachalam, R. Jayavel and I. Vetha Potheher, A study on the synthesis and characterization of $CoMn_2O_4$ electrode material for supercapacitor applications, *J. Mater. Sci.: Mater. Electron.*, 2016, **27**(5), 4653–4658.

37 S. Xu, S. Gong, H. Jiang, P. H. Shi, Q. J. Xu and Y. L. Min, Z-scheme heterojunction through interface engineering for broad spectrum photocatalytic water splitting, *Appl. Catal., B*, 2020, **267**, 118661.

38 S. W. Luo, R. Gu, P. H. Shi, Q. J. Xu and Y. L. Min, Π-Π interaction boosts catalytic oxygen evolution by self-supporting metal-organic frameworks, *J. Power Sources*, 2020, **448**, 227406.

39 S. Q. Gong, Z. J. Jiang, P. H. Shi, J. C. Fan and Y. L. Min, Noble-metal-free heterostructure for efficient hydrogen evolution in visible region: Molybdenum nitride/ultrathin graphitic carbon nitride, *Appl. Catal., B*, 2018, **238**, 318–327.

40 T. Wu, Y. Ma, Z. B. Qu, J. C. Fan, Q. X. Li, P. H. Shi, J. C. Fan and Y. L. Min, Black phosphorus-graphene heterostructure-supported Pd nanoparticles with superior activity and stability for ethanol electro-oxidation, *ACS Appl. Mater. Interfaces*, 2019, **11**(5), 5136–5145.

41 K. Lu, Z. J. Min, J. X. Qin, P. H. Shi, J. F. Wu, J. C. Fan, Y. L. Min and Q. J. Xu, Preparation of nitrogen self-doped hierarchical porous carbon with rapid-freezing support for cooperative pollutant adsorption and catalytic oxidation of persulfate, *Sci. Total Environ.*, 2020, 142282.

42 X. Wang, X. F. Zhang, L. Dai, H. Guo, P. H. Shi, Y. L. Min and Q. J. Xu, Recycling the Cathode Scrap of Spent Lithium-Ion Batteries as an Easily Recoverable Peroxymonosulfate Catalyst with Enhanced Catalytic Performance, *ACS Sustainable Chem. Eng.*, 2020, **8**(30), 11337–11347.

43 J. Z. Zhang, S. Zhu, Y. L. Min and Q. J. Xu, Mn-doped perovskite-type oxide $LaFeO_3$ as highly active and durable bifunctional electrocatalysts for oxygen electrode reactions, *Front. Mater. Sci.*, 2020, 1–10.

44 J. Zhao and R. F. Peng, Gas-Solid Two-Phase Flow Synthesis Equipment: A New Method for Continuous, Large-Scale Preparation of Metal-Organic Frameworks with No Solvent, *Ind. Eng. Chem. Res.*, 2020, **59**(35), 15791–15795.

45 J. Zhao, B. Jin and R. F. Peng, New Core-Shell Hybrid Material IR-MOF3@COF-LZU1 for highly efficient-visible-light photocatalyst-degrading nitro-aromatic explosives, *Langmuir*, 2020, **36**, 5665–5670.